



PCCP

Differential Hysteresis Scanning of Non-Templated Monomodal Amorphous Aerogels

Journal:	<i>Physical Chemistry Chemical Physics</i>
Manuscript ID	CP-ART-10-2020-005520.R1
Article Type:	Paper
Date Submitted by the Author:	18-Feb-2021
Complete List of Authors:	Taheri, Poroshat; The University of Texas at Arlington, Chemistry and Biochemistry Lang, John; The University of Texas at Arlington, Department of Chemistry and Biochemistry Kenvin, Jeff; Micromeritics, Science Kroll, Peter; The University of Texas at Arlington, Department of Chemistry and Biochemistry

SCHOLARONE™
Manuscripts

ARTICLE

Differential Hysteresis Scanning of Non-Templated Monomodal Amorphous Aerogels

Poroshat Taheri,^a John C. Lang^a, Jeffrey Kenvin^b and Peter Kroll,^{*a}Received 22nd October 2020,
Accepted 00th January 20xx

DOI: 10.1039/x0xx00000x

We perform Differential Hysteresis Scanning (DHS) Porosimetry of amorphous silicon oxycarbide aerogels to quantify hierarchical connectivity in these porous materials. We contrast high-resolution argon sorption scanning isotherms of samples obtained through a non-templated synthesis using different solvents, and characterize respective changes after calcination at 1000 °C. The multi-scan DHS data sets are analyzed through non-negative least-squares deconvolution using a kernel of theoretically derived isotherms for a selection of hierarchical geometries using non-local density functional theory (NL-DFT). We obtain two-dimensional contour plots that characterize mesopores according to the ratio between pore diameter and its connecting window. Combined information from DHS and complementary BET and BJH approaches reveals one system with monomodal distribution both in pore diameters and in window diameters. Hence, this amorphous material exhibits a uniformity usually only observed for crystalline systems. We demonstrate that DHS analysis provides quantitative data analyzing the hierarchical structure of mesoporous materials and unlocks pathways towards tailored materials with control of surface heterogeneity, localization, and sequential accessibility – even for amorphous systems.

1. Introduction

Quantitative assessment of gas sorption using simple gases has matured from its beginnings in the early 1900's to become a conventional technique for investigating surface heterogeneity, structural morphology and thermodynamics of porous materials.^{1, 2} This technology has been applied effectively for studies of materials with both meso- (~ 2-50 nm) and micro- (< ~ 2nm) pores. Correspondences between characteristics of gas sorption isotherms and pore morphologies have been analyzed and systematized in IUPAC conventions with a specific recommendation for the usage of argon adsorption isotherms for materials with pores less than 2nm in size.^{3, 4} Based on phenomenological models and adsorbed volumes, surface areas can be established. On condensation of gas at higher pressures, the behavior of the adsorbed fluid provides information regarding pore volumes from which pore sizes, geometries and connectivity can be inferred. Staple methods to characterize meso-porous systems include Brunauer–Emmett–Teller (BET) analysis for calculation of specific surface area (SSA) and surface energetics,⁵ and Barrett-Joyner-Halenda (BJH) analysis for determining distributions of average pore volumes and sizes.⁶ Early refinements of these approaches were contributed by statistical thermodynamic interpretation of, and calorimetric data on, adsorption energetics,^{2, 7-10} estimations of

the adsorbed thickness of multilayer films,¹¹⁻¹³ improved understanding of ordering in condensed phases,^{14, 15} and appreciation of the detailed structural information from observations of capillary condensation and adsorption hysteresis.¹⁶

More recently, with improvements in computational modeling and the convergence of results from density functional, molecular dynamics and Monte Carlo methods, statistical mechanical approaches have successfully investigated the influences of ever more complicated pore architectures, pore dimensionality, surface heterogeneity and molecular interactions in systems undergoing class 1 film growth.^{17, 18} Modeling of both structure and thermodynamics of porous materials of greater complexity have improved interpretations of experimental evaluations.¹⁹⁻²² Non-local density functional theory (NLDF) is an efficient statistical thermodynamic approach for analyzing the population density of a system of molecules interacting with a surface.²³⁻²⁷ It has been used to describe the gradual buildup, and loss of solid-packing-like ordering, of multilayers in film formation and condensation as originally depicted in the BET model of adsorption. This method has become an efficient tool for analyzing and interpreting porous structures.^{22, 28, 29} Complementary theoretical and experimental studies of well-characterized, highly ordered, templated materials, such as M41S,³⁰ have validated this theoretical foundation of gas sorption used for pore characterization.³¹

Cavities in a material can attain a variety of shapes and sizes, narrowly or broadly distributed, having a hierarchy of interconnectivity all influenced by the chemistry of the material and its preparation. Often contrasting and complementary structures are generated, dependent on whether the synthesis

^a Department of Chemistry & Biochemistry, The University of Texas at Arlington, Arlington, TX 76019 USA.

^b Micromeritics Instrument Corporation, 4356 Communications Drive, Norcross, Georgia 30093, USA.

† Electronic Supplementary Information (ESI) with additional discussion available. See DOI: 10.1039/x0xx00000x

is a bottom-up arrangements of coalescing particles, i.e. the structural building blocks, or a top-down removal of fragments from an existing structure.³² Cavities may be linked to each other creating an intrinsic network of pores. These structural features, combined with different surface heterogeneity, can impact adsorption and desorption differently. In particular, hysteresis in gas sorption data indicates the presence of constrictions that regulate desorption from larger interconnected cavities, under control of the pore hierarchy.³²⁻³⁵ There are few techniques to map the hierarchy of porous materials. X-ray tomography can be used for studying macroporous systems with a resolution of about 1 μm .³⁶⁻³⁸ Transmission electron microscopy (TEM) is applied for ordered microporous materials such as zeolites and can reach a resolution of ~ 1 nm.^{39, 40} Early approaches of analyzing hysteresis loops observed in gas sorption focused on uniformly sized mesoporous systems.⁴¹⁻⁴⁴ In recent studies the Differential Hysteresis Scanning (DHS) technique was developed by one of us and applied to study pore hierarchy in crystalline faujasites.²¹

22

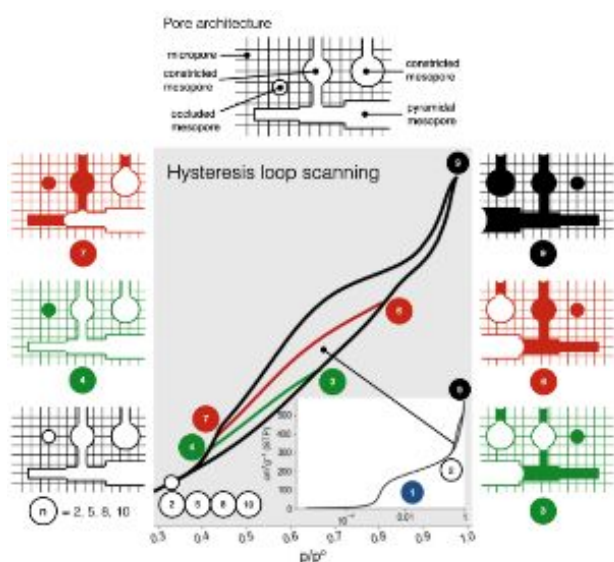


Figure 1: Schematized sequence of filling and emptying of complex pores accompanying the sequential differential hysteresis scans (DHS).

The DHS technique is a rigorous analysis of the hysteresis loops and subloops observed when scanning the adsorption and desorption branches of an isotherm. Scanning isotherms may be obtained by several methods. The DHS technique analyses the hysteresis subloops formed by sequential increasing partial saturation of the pore network. An example of hysteresis subloops is illustrated in Figure 1. The technique uses the difference between increasing levels of saturation from the component scans as input for the modelling. The systematic filling and emptying of the pores of the partially saturated network is suggested by the sequential numbering of the individual scans in Figure 1. The desorption branch of the isotherm is controlled by the dimension of the entrance to a pore, herein referred to as the window. The adsorption branch is

influenced by the dimension of the larger cavity, referred to as the pore size. The DHS technique utilizes adsorption and desorption branches of the scans to establish the nature and relative distribution of the controlling windows and their connected pores. NLDFT models are employed to calculate the changes in pore size distributions required for modeling accurately the isotherm scans measured experimentally.

In this study we apply the DHS technique to address for the first time the structural heterogeneity in silicon oxycarbide disordered aerogels. With this method quantitative assessment of the distribution of pore sizes and geometries, and their morphological changes on calcination, have been determined for these heterogeneous hierarchical systems.

Silicon oxycarbide (SiCO) is a versatile material with modifiable functional properties dependent on synthesis and processing.⁴⁵⁻⁴⁷ Porous SiCO materials have been fabricated through a variety of methods and their diverse applications explored,^{47, 48} including as membranes for gas separation,⁴⁹ as macroporous hydrophobic fibers for environmental remediation,⁵⁰ and as anodes for lithium ion storage.⁵¹ SiCO aerogels are synthesized from polymers or molecular precursors, have been processed with various heat treatments at elevated temperatures, and resulting porosities have been characterized.⁵²⁻⁵⁶ For further development of these porous materials in more demanding applications – e.g., for drug delivery,⁵⁷⁻⁵⁹ separations,⁴⁹ and catalyst support⁶⁰ – knowledge and control of their pore hierarchy will be required. Here in this paper we deliver new insight into the pore architecture of SiCO aerogels using a combination of both conventional gas sorption and Differential Hysteresis Scanning (DHS).

2. Experimental

2.1 Synthetic procedures

We synthesized SiCO aerogels by cross-linking polymethylhydrosiloxane (PMHS) with divinylbenzene (DVB) in excess solvent, either cyclohexane or acetone, via hydrosilylation.⁵³ PMHS (MW \sim 1900, CAS: 63148-57-2), DVB (technical grade, 80%, CAS: 1321-74-0) and the Karstedt's catalyst (platinum divinylmethylsiloxane complex), \sim 2% in xylene (CAS: 68478-92-2) were purchased from Sigma-Aldrich, Saint Louis, MO, USA. Acetone (CAS: 67-64-1) was bought from Macron Fine Chemicals, VWR, Radnor, PA, USA, and cyclohexane (CAS: 110-82-7) was acquired from Fisher Scientific, USA. We prepared a solution of a 1:2 mixture (by mass) of PMHS and DVB in 85% (by volume) of either cyclohexane or acetone as solvents. We added 10 μL of Karstedt's catalyst to each mixture, transferred it into a pressure reactor, and placed it in an oven at 150 $^{\circ}\text{C}$ for 6 hours, a temperature above the 1 atm boiling point of the solvent. Thereafter, the sample was gently removed from the reactor vessel and soaked repetitively for 6 hours, washing five times in the solvent used for the synthesis, adequate for removing all the catalyst and terminating the reaction.

In the next step, the sample was transferred carefully into a cylindrical CO_2 -reactor of in-house design. There are two glass

windows at either end to permit visual inspection, useful for observing and controlling solvent exchange with liquid CO₂ and for monitoring the supercritical drying process. Each gel was washed with liquid CO₂ at 4 °C twice per day for a total of 10 solvent exchanges. Subsequently, the final step of the drying process was performed over a 10-hour period by slowly increasing the temperature to 45 °C at a pressure of 100 - 110 bar. After supercritical drying in a CO₂-reactor we recovered **polymeric aerogels (pa)**. The **polymeric aerogel (pa)** synthesized in cyclohexane was labeled **pa-c** and the **polymeric aerogel (pa)** synthesized in acetone was labeled **pa-a**. Extracting the solvent in the supercritical dryer led to shrinkage of the samples. Therefore, the height and diameter of the (almost) cylindrical **pa-c** and **pa-a** aerogels were measured before and after supercritical drying using a graph paper. Bulk densities of samples were calculated using measured volume and mass of **pa-c** and **pa-a**. The linear shrinkage was 37% for **pa-c** and 18% for **pa-a** after supercritical drying. Their bulk densities were 0.7 g cm⁻³ for **pa-c** whereas 0.3 g cm⁻³ for **pa-a** respectively, a ratio comparable to the inverse of their ratio of total pore volumes. Subsequent annealing to 1000 °C in flowing nitrogen transformed these polymeric aerogels into their **ceramic aerogel analogs (ca)**. The ramp from room temperature to 400 °C used a heating rate of 5 °C min⁻¹, and then temperature was kept for 2 hours at 400 °C. Thereafter, the sample was heated from 400 °C to 1000 °C with a heating rate of 5 °C min⁻¹, after which temperature was held at 1000 °C for 4 hours. The furnace was then switched off and samples allowed cooling to room temperature. The **ceramic aerogel (ca)** synthesized in cyclohexane was labeled **ca-c** and the **ceramic aerogel (ca)** synthesized in acetone was labeled **ca-a**. We have chosen this system because, while dense SiCO ceramics synthesized from polymeric PMHS-DVB are well-known and well-characterized,^{47, 55, 61} their pore morphology, and attributes controlling it, remain to be fully elucidated.^{53, 62, 63}

2.2 Scanning Electron Microscopy (SEM)

We characterized the pre-ceramic aerogels using Scanning Electron Microscopy (Hitachi S-4800 II FE SEM) by looking at fracture surfaces of **pa-c**, **pa-a**, **ca-c**, and **ca-a**. Due to the low electrical conductivity of the **pa-c** and **pa-a** sample, they were coated with silver (CrC-100 Sputtering System) (Plasma Sciences Inc, Ooltewah, TN). For particle size determination we used ImageJ software.⁶⁴ In the SEM image 145 pixels correspond to 1 μm. For estimating average particle size, we measured the diameters of for 25 particles with distinct boundaries in each SEM image.

2.3 Porosity

Nitrogen (at 77 K) and argon (at 87 K) sorption characteristics were measured using a Micromeritics ASAP 2020 porosimeter. We applied the Brunauer–Emmett–Teller (BET) analysis for calculating specific surface area (SSA),⁵ and Barrett–Joyner–Halenda (BJH) procedure using desorption branch of the isotherms to estimate their pore size distribution (PSD).⁶ The total pore volume (TPV) was taken directly from the maximum of the isotherm. BJH pore size distribution can be unreliable for pores lower than 6 nm.⁶⁵ Therefore, the pore size distribution

graphs have the lower limit of 6 nm. All isotherms shown in Figures 5 and 6 are classified as Type IV (a) according to IUPAC.⁴

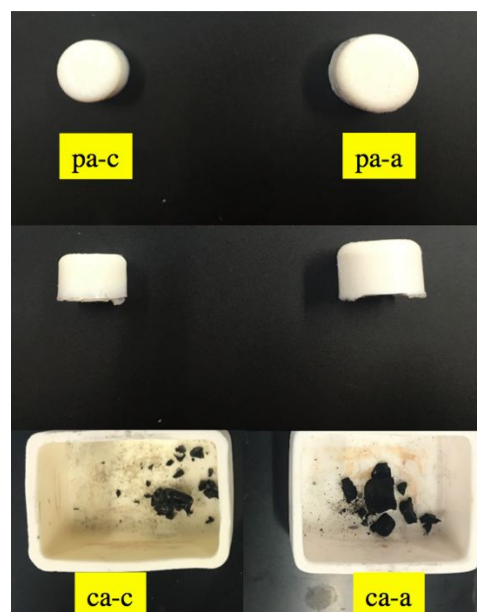
2.4 Differential Hysteresis Scanning (DHS)

We carried out Differential Hysteresis Scanning (DHS) measurements by high-resolution argon sorption on the pre-ceramic **pa-a** and **pa-c** as well as annealed **ca-a** and **ca-c** using Micromeritics ASAP 2020. Scanning isotherms were acquired by incrementally increasing the partial saturation of the sample followed by a high-resolution desorption (Figure 5). In total, 14 scans for each sample were collected. The pressure table for each sample was designed individually based on the maximum quantity of gas adsorbed at a P/P₀ of 0.98 so that 14 scans were adequate to cover the whole hysteresis region uniformly. A completed DHS experiment of a single sample took approximately 4 days. The distribution of pore window sizes and pore diameters as well as incremental pore volumes were calculated by the system software using non-negative least-squares (NNLS) deconvolution of the scanning and differential isotherms based on the weightings from a kernel of model adsorption isotherms generated from the Tarazona version of the NLDFT with specific Lennard–Jones solid–fluid (sf) and fluid–fluid (ff) parameters for the sample material.²⁵ Here, three basic types of mesopores are considered according to the relative diameter of the window: pyramidal ($d_{\text{pore}} > 2 \text{ nm}$, $d_{\text{win}} > d_{\text{pore}}$), constricted ($d_{\text{win}} > 2 \text{ nm}$, $d_{\text{win}} < d_{\text{pore}}$), and occluded ($d_{\text{win}} < 1 \text{ nm}$, $d_{\text{win}} < d_{\text{pore}}/10$). That the domains for the DHS contour plots may not extend to these limits reflects the size of the hysteresis loops under investigation.

3. Results and discussion

3.1 SEM Analysis: Network's Constituent Colloidal Particles

The polymeric aerogels (Figure 2, top) appear milky white in color while, with reduction occurring on annealing, the ceramic aerogels turn black (Figure 2, bottom).



ARTICLE

Physical Chemistry – Chemical Physics

Figure 2: Pictures of polymeric (top) and ceramic (bottom) SiCO aerogels. **pa-a** (right) and **pa-c** (left) are shown from top and side angle. **ca-a** (right) and **ca-c** (left) as received after annealing at 1000 °C in nitrogen.

The SEM micrographs in Figure 3 show that microstructures of the polymeric aerogels consist of almost spherical colloidal particles. Particles in the annealed ceramics, **pa-c**'s, are fused closely together without significant space between the individual particles. In contrast, packing of spheres in **pa-a** is less dense, with more open spaces and large cavities visible between individual and paired or fused spheres. We determined an average particle size of 160 ± 26 nm and 200 ± 31 nm for **pa-c** and **pa-a**, respectively. After annealing, the **ca** particles have coalesced, and while it is possible to identify large holes in the surface, it is impossible to differentiate individual particles. Note that the resolution of the electron micrographs does not allow examination of the mesoporosity in the aerogels.

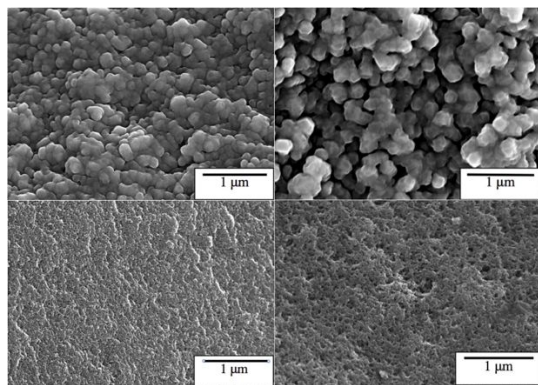


Figure 3. SEM micrographs of pre-ceramic polymeric aerogels prepared in acetone **pa-a** (right, top), and prepared in cyclohexane **pa-c** (left, top); the annealed ceramic resulting from the aerogel prepared in acetone, **ca-a** (right, bottom), and the ceramic prepared in cyclohexane **ca-c** (left, bottom) at 30K resolution.

3.2 BET and BJH Analysis of Isotherms

Gas sorption isotherms for polymeric and ceramic aerogels obtained using nitrogen and argon are shown in Figure 4a, eight isotherms in all. Previous porosity studies of SiCO used nitrogen as sorbent gas.^{53, 63} For each of the four samples, a comparison between the Ar and N₂ sorption data is provided, illustrating the consistency between adsorbates, and thereby relating our observations to the previous work. Figure 4b provides the Barrett-Joyner-Halenda (BJH) pore size distributions derived from the desorption branches of the isotherms,⁶ the desorption illustrating the greater contrasts since differences in pore interconnectivity augments the size distinctions. We note that BJH pore size distributions can be unreliable for pores diameters smaller than 6 nm,⁶⁵ and other approaches exist to characterize smaller pores (e.g. DFT and Horvath-Kawazoe methods).^{25, 26, 66, 67} Pore sizes observed here for both adsorption and desorption are above this limit, however, and BJH analysis is expected to be reliable.

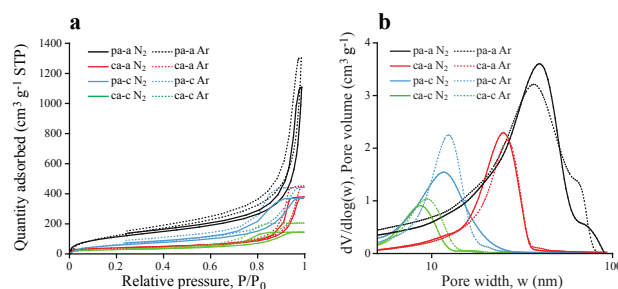


Figure 4. Isotherms and BJH pore size distributions of **pa-c**, **pa-a**, **ca-c**, and **ca-a**. **a:** nitrogen sorption (continuous line) and argon sorption (dash line) isotherms of **pa-c**, **pa-a**, **ca-c**, and **ca-a**. **b:** BJH pore size distributions of the nitrogen desorption (continuous line) and argon desorption (dash line) of the **pa-c**, **pa-a**, **ca-c**, and **ca-a**. Note, the pore width spans 6 to 100 nm, appropriate for the BJH analysis of these samples.

Total pore volumes and shapes of sorption isotherms of aerogels synthesized in cyclohexane are clearly different from those synthesized in acetone, regardless of adsorbate used or whether the sample was annealed or not. While all isotherms of Figure 3A indicate a modest level of micropores and are characterized as Type IV(a) according to IUPAC nomenclature,⁴ the broader hysteresis loop in the cyclohexane-derived aerogels differentiates them as Type H2(b), while the narrow, more vertical loop for aerogels synthesized in acetone accord most consistently with Type H1. In general, hysteresis loops of Type IV(a) are attributable to capillary condensation in the mesopore regime where the capillary window is of more variable dimension.⁴ The H1-Type hysteresis can be ascribed best to materials whose porosity consists of a narrow range of mesopores where the neck of these pores is only slightly narrowed. Hysteresis of Type H2 (b) appears in the isotherm of materials consisting of a greater differential in neck and pore size distributions. In applications this can result in not only a network or percolation effect, where transverse transport can be enhanced,⁶⁸ but also pore-blocking and, with processing such as annealing, cavitation or collapse.⁴ We observe that isotherms of both **pa-c** and **pa-a** exhibit an open-ended hysteresis loop at about $p/p_0 \approx 0.22$. This may be attributable to micropore windows connected to mesopores, effectively producing transient pore blocking with slower diffusion kinetics. Perhaps more likely, the open loop may be the consequence of the temperature- and window-dependent capillary evaporation from a receding meniscus.⁶⁹ Similar behavior has been observed in shale hydrocarbons,⁷⁰ which show low-pressure hysteresis (LPH).⁷¹ The open-ended isotherms of **pa-c** and **pa-a** were observed in a previous study from our group.⁶³ In contrast, both hysteresis loops of **ca-c** and **ca-a** isotherms are closed by $p/p_0 \approx 0.5$, presumably because the micropores collapsed during annealing.

Comparing the influence of solvent on the isotherms for the polymeric aerogels, we find that the total quantity of gas (either N₂ or Ar) adsorbed by **pa-a** is three times larger than by **pa-c**. This reflects, shown in Table 1, the larger total pore volume in

pa-a ($\sim 1.8 \text{ cm}^3 \text{ g}^{-1}$) in comparison to **pa-c** ($\sim 0.6 \text{ cm}^3 \text{ g}^{-1}$), or alternatively the considerably lower density of **pa-a**. The changes in the BET “C” parameter support both greater amount of surface organic component in the polymeric aerogel, which apparently is not altered appreciably by the different solvents, and its loss on annealing.⁷²⁻⁷⁴ The argon adsorption suggests there may be less organic lost by the aerogel prepared in acetone, surprising since its pores are larger than aerogel prepared in cyclohexane. The average SSA of **pa-a** ($\sim 439 \text{ m}^2 \text{ g}^{-1}$), which is attained consistently for both nitrogen and argon sorption data, is approximately twice as large as the SSA of **pa-c** ($\sim 218 \text{ m}^2 \text{ g}^{-1}$).

Clearly, the hysteresis distorts the pore size distribution as portrayed in Figure 4b. For the classical cylindrical model and from the experimental values in Table 1, the ratios of pore volumes to pore areas, averaged over both adsorbates, would suggest the radii of the larger pores in **pa-a** could be expected to be only about 1.4 times those of **pa-c**. This is consistent with the area of **pa-a** being about twice that of **pa-c**. However, the

ratio of the most probable pore radii indicated by the BJH analysis in Figure 4b is greater than 3. The BJH analysis of the hysteresis here overemphasizes the amount of the smaller pores in **pa-c**. So, while the trends for smaller size pores in the aerogels synthesized in cyclohexane, observed in the isotherms, are borne out, the quantitation is in question. This will be addressed below when discussing the results of the DHS. Similar trends are observed when contrasting the data of the ceramic aerogels produced by annealing the samples from the different solvents. The isotherms and hysteresis loops of **ca-a** and **ca-c** show consistent and proportional reductions in their properties: the amounts of adsorbed gas, pore sizes and distributions, total pore volumes and SSA's are reported in Table 1. Here, also, the ratios indicate the BJH analysis overestimates the ratio of pore radii of **ca-a** to **ca-c**, though the disparity is slightly reduced.

Table 1. BET-determined specific surface area (SSA) was computed from the adsorption at monolayer coverage, the value of Q_m converted from $\text{cm}^3 \text{ g}^{-1}$ at STP. The BET-determined unitless “C” parameter, computed from the isotherm transform, is a measure of adsorbate/adsorbent interaction. The total pore volume (TPV) was established from the maximum in the gas adsorption isotherm, assuming the fluid at P/P_0 of 1 is all liquid. These values for the SiCO aerogels were established from adsorption of nitrogen (at 77 K) and argon (at 87 K). The approximate bulk density in the last column is provided for comparison. Because of the fragility of **ca-a** and **ca-c**, their bulk densities were not evaluated.

Sample	SSA		BET C		TPV		ρ (bulk) (g cm^{-3})
	N_2 ($\text{m}^2 \text{ g}^{-1}$)	Ar ($\text{m}^2 \text{ g}^{-1}$)	N_2	Ar	N_2 ($\text{cm}^3 \text{ g}^{-1}$)	Ar ($\text{cm}^3 \text{ g}^{-1}$)	
pa-c	219	217	47.1	29.0	0.61	0.57	0.7
ca-c	95	100	148.7	112.6	0.22	0.27	-
pa-a	414	463	47.3	28.0	1.7	1.7	0.3
ca-a	132	116	146.8	76.3	0.58	0.58	-

pore size ($d_{\text{win}} \ll d_{\text{pore}}$, $d_{\text{win}} < 2 \text{ nm}$). The relation between the diameter of the pore (d_{pore}) and

3.3 Isotherm Scanning and DHS Analysis

Four sets of multiple high-resolution argon sorption isotherm scans are shown in Figure 5, a-d. Each set constitutes the Differential Hysteresis Scanning (DHS) experimental measurements for the sample indicated. Each isotherm is shown decomposed into fourteen component scans, the current maximum for the software. The measured isotherm is effectively treated as a composite response for a collection of pores with a variety of geometries, such as suggested in Figure 1.

The results of the DHS analysis may then be used to distinguish three core geometric classes of mesopores according to the relative dimensions of their pores and windows (bottlenecks): (i) non-restrictive pyramidal pores with a window size equivalent to or larger than the pore size ($d_{\text{win}} \geq d_{\text{pore}}$), (ii) constricted pores with a window smaller than the pore size ($d_{\text{win}} < d_{\text{pore}}$ and d_{win} is of mesopore dimension), and (iii) a third type, a special case of constricted pores, with essentially occluded pores in which a micropore window is much smaller than the

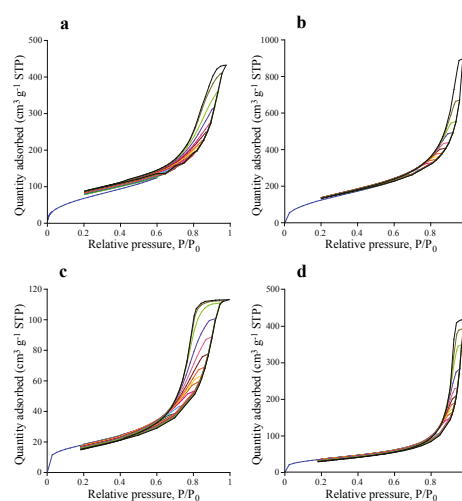


Figure 5. DHS Ar sorption at 87 K; **a.** on **pa-c**; **b.** on **pa-a**; **c.** on **ca-c**; and **d.** on **ca-a**. The fourteen sorption scans for each

sample are the input data for the corresponding DHS analysis provided in Figure 6.

diameter of its connected window (d_{win}) for the aerogels is plotted in two-dimensional (2D) contour plots in Figure 6. White lines segregate the 2D plane into regions corresponding to pyramidal, constricted, and occluded mesopores. As illustrated,

sets of pores with the same ratio of pore to window diameters follow diagonals, and those sets of ratios defining the three types of regions occupy the designated areas. The region designating the pyramidal pores complies with a functional description in that, for large pores with window diameters slightly narrower than the pores, their desorption will be little constrained by the modest narrowing.

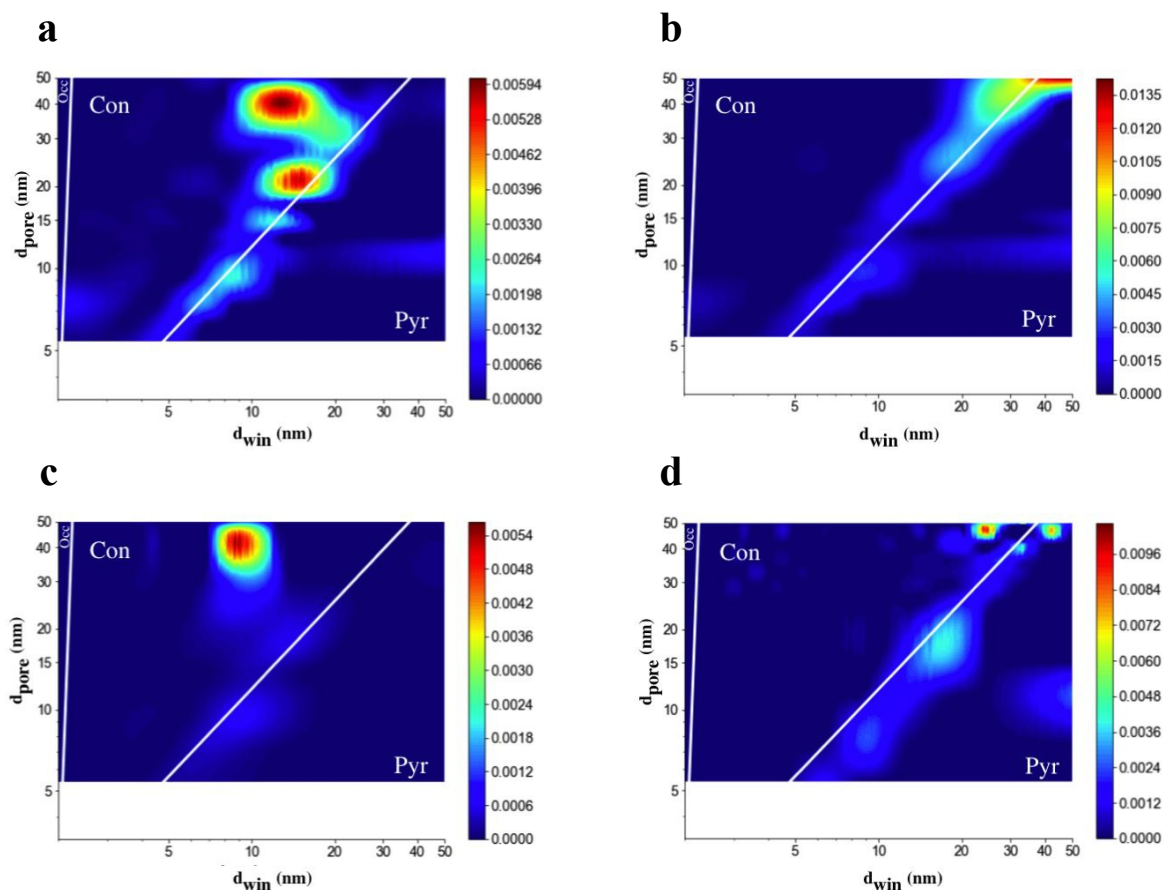


Figure 6. Two-dimensional (2D) contour plots characterizing the relation between the diameter of the pore and that of its connected window derived via DHS from Ar sorption at 87 K. Polymeric aerogels are in the top row, **pa-c** (a), **pa-a** (b), and ceramic aerogels in the bottom row, **ca-c** (c) and **ca-d** (d). The color scale of each sample is normalized to its total mesopore volume. White lines split the 2D plane to into pyramidal (Pyr), constricted (Con), and occluded (Occ) mesopore areas.

Figure 6 exhibits a striking difference between the relative pore and window diameters for the aerogels synthesized in cyclohexane before and after annealing, **pa-c** (Fig 6a) and **ca-c** (Fig 6c). Simply, before the annealing there is a bimodal distribution of pore sizes, at approximately a 2:1 ratio of pore sizes, each with approximately the same window dimension. After annealing the smaller pores have disappeared while the larger ones have remained about the same size, and the window area contracted to just 36% of the original size. In detail, for **pa-c** prior to annealing we observe two strong maxima (indicated by red color) and three minor maxima, the latter in sum are but a small fraction of pores. One of the strong maxima is centered at a pore diameter of 41.4 nm with a pore window size of 13.2 nm, and the other, slightly less pronounced one, centered at 21.6 nm with a pore window size of 14.6 nm.

Therefore, the DHS analysis reveals essentially a bimodal distribution of pore sizes. We emphasize that this bimodal distribution in pore size is not resolved in the BJH analysis of the original isotherm. Moreover, the DHS-derived pore diameters of the peak at 12 nm found in the distribution derived from BJH analysis (see Figure 4b). We had noted previously that quantitation of BJH pore sizes for **pa-c** is in question, as is common when hysteresis is significant — and the DHS data provides insight into this BJH overestimation of smaller pores. Analyzing the two strong maxima further, we find that the ratio of pore window diameter to pore diameter for the larger pores is 0.32, while that ratio for the smaller pores is 0.68. Hence, larger pores are considerably more restricted than smaller pores. Consequently, in Figure 6 the cohort with the larger

pores is located further from the white diagonal, which represents the boundary between the constricted and pyramidal geometry.

DHS analysis of **ca-c**, the ceramic counterpart of **pa-c** annealed at 1000°C, indicates just one strong maximum with average pore diameter of 43.2 nm and a pore window size of 9.1 nm. Thus, while the pore diameter for the larger pores changed only insignificantly, both the central window diameter and its range of diameters decreased considerably. The average window sizes were reduced from 14.6 nm to 9.1 by 30 %, the range in sizes from 5.8 nm to 3.3 nm even stronger, by 43%. The most surprising and notable change upon annealing, however, is the complete “disappearance” of smaller pores. Because it is not clear whether these pores have collapsed completely or are just sufficiently occluded that there is effectively no adsorption, this effect is under current investigation. But clearly, the more vulnerable to collapse were those of smaller size.

The bimodal distribution itself is of interest since it has been reported to occur in analogous systems of tightly packed spheres, there for sol-gel systems.⁷⁵⁻⁷⁹ The occurrence has been attributed to intra- and inter-particulate pores. If that be the case here, it seems highly unlikely that both populations of pores should have windows of such similar size, unless they are in some way connected. Supposing that they are connected, then either the large pores or the small pores would be connected first to the window. Since, however, the small pores collapse on annealing, yet the large pores are still accessible, the only possibility is that the window is connected to the large pores first, that in turn are connected to the smaller pores. This picture is consistent with the synthetic procedure in which the particles grow, then agglomerate, with just a window opening onto the larger interparticle spaces, which in turn are connected to the intraparticle pores. As discussed further in the Supporting Information the **pa-c** samples before annealing appear to have a monomodal window distribution with a bimodal pore size distribution and following annealing monomodal window and pore distributions [cf. §1.3 Supporting Information].

In contrast to results obtained for the samples synthesized in cyclohexane, yet consistent with material having Type H1 isotherms that increase abruptly at high pressures, those synthesized in acetone, **pa-a** and **ca-a**, exhibit distributions skewed to large pore diameters. These sizes, anticipated from the BJH analysis in Figure 4b, are in fact so large that the pore sizes appear to lie outside the range of the DHS analysis. There appears to be little evidence for constricted geometries, since most of the distributions lie on or near the line of equal pore and window dimensions. This is consistent with the observation of a large total pore volume, with correspondingly low density, and with the very narrow hysteresis loop. DHS analysis of **ca-a** shown in Figure 6d does suggest, however, that annealing the sample may be generating some level of constriction.

A quantitative breakdown of the amount of the different types of pore geometries for the four materials investigated is provided in Table 2. The amount of each of these three types of pore are quantified in terms of adsorbed volume, in cm³g⁻¹ STP. The total mesopore volume of pores analyzed by the DHS

composite hysteresis loop is the sum of these three types of mesopores. For each of the samples the predominant pore type is constricted. The most porous and least dense sample, **pa-a**, has the greatest volume of constricted mesopores. Approximately 56% of that volume is retained in **ca-a** obtained after annealing. The denser sample, **pa-c** produced in cyclohexane, has only 30% of the total mesopore volume of **pa-a**. This sample shows a remarkable loss in mesoporosity after annealing, with the major type of mesopore losing 92% of its volume. These quantitative evaluations reflect the observations based on the graphical analysis described above [cf. §1.2 Supporting Information].

Table 2. The percent of each pore type for all four preparations, quantified by the DHS software for each sample. The data are normalized to the total volume of porosity of **pa-a**, set to 100%. This provides an estimate of the relative amount of each type of mesopore across the set of samples. SI provides more detail.

Sample	% Pyr	% Con	% Occ
pa-c	2.7	26.3	1.2
ca-c	0.4	2.0	0.2
pa-a	27.8	69.1	3.1
ca-a	10.7	38.4	4.7

4. Conclusions

To our knowledge, this investigation is the first application of Differential Hysteresis Scanning (DHS) porosimetry to assess pore geometry and connectivity in an amorphous aerogel. We have illustrated how DHS augments and complements the structural information from electron microscopy and more classical porosimetry, providing a fuller description of the range of prevailing structures and their hierarchical interconnections. The technology, in conjunction with other assessments, reveals the significant changes occurring in pore and surface characteristics resulting from modification of the kinetics and thermodynamics associated with the synthetic procedure and subsequent processing. Knowledge of the hierarchical structure can assist significantly in meeting the design requirements for diverse applications, notably in control of surface heterogeneity, localization, and sequential accessibility. Specifically, we have illustrated how a simple change in solvent in the synthesis of an aerogel can result in a system with monomodal distribution both in pore diameters and in window diameters. Such uniformity is characteristic for crystalline systems, and is shown here to occur even in a non-crystalline amorphous aerogel. Materials of this kind will exhibit homogeneous conditions and confinement for molecules and should be valuable in applications ranging from catalysis to drug delivery.

Conflicts of interest

There are no conflicts to declare.

Acknowledgements

This work was supported by the National Science Foundation (NSF) through award CMMI-1634448 and through a Non-Academic Research Internship for Graduate Students (IN-TERN) for PT.

References

- J. W. McBain, *London, Edinburgh, and Dublin Philosophical Magazine and Journal of Science*, 1909, **18**, 916-935.
- S. Gregg and K. Sing, *Adsorption, surface area and porosity*. Academic Press, London, 1982.
- K. S. W. Sing, *Pure Appl. Chem.*, 1985, **57**, 603.
- M. Thommes, K. Kaneko, V. Neimark Alexander, P. Olivier James, F. Rodriguez-Reinoso, J. Rouquerol and S. W. Sing Kenneth, *Pure Appl. Chem.*, 2015, **87**, 1051.
- S. Brunauer, P. H. Emmett and E. Teller, *J. Am. Chem. Soc.*, 1938, **60**, 309-319.
- E. P. Barrett, L. G. Joyner and P. P. Halenda, *J. Am. Chem. Soc.*, 1951, **73**, 373-380.
- S. R. H. Fowler and E. A. Guggenheim, *Statistical Thermodynamics. A Version of Statistical Mechanics [by RH Fowler] for Students of Physics and Chemistry*, Cambridge, 1939.
- T. L. Hill, *J. Chem. Phys.*, 1946, **14**, 263-267.
- T. L. Hill, *J. Chem. Phys.*, 1949, **17**, 668-669.
- S. Ross and J. Olivier, *On Physical Adsorption*, Wiley and Sons, Interscience Division of John Wiley & Sons, New York, 1964.
- J. Frenkel, *Kinetic Theory of Liquids*, Oxford University Press, 1946.
- G. Halsey, *Journal of Chemical Physics*, 1948, **16**, 931-937.
- C. Pierce, *Journal of Physical Chemistry*, 1960, **64**, 1184-1187.
- W. D. Harkins and G. Jura, *J. Am. Chem. Soc.*, 1944, **66**, 1366-1373.
- M. Kruk, M. Jaroniec and A. Sayari, *Langmuir*, 1997, **13**, 6267-6273.
- D. Everett, in *The Solid-Gas Interface*, ed. E. Flood, Marcel Dekker, Inc., New York, 1967, vol. 2, ch. 36, pp. 1055-1113.
- L. D. Gelb, K. Gubbins, R. Radhakrishnan and M. Sliwinski-Bartkowiak, *Rep. Prog. Phys.*, 1999, **62**, 1573.
- J. Dash, *Le Journal de Physique Colloques*, 1977, **38**, C4-201-C204-206.
- J. Kenvin, J. Jagiello, S. Mitchell and J. Pérez-Ramírez, *Langmuir*, 2015, **31**, 1242-1247.
- M. Thommes, *Chem. Ing. Tech.*, 2010, **82**, 1059-1073.
- J. Kenvin, S. Mitchell, M. Sterling, R. Warringham, T. C. Keller, P. Crivelli, J. Jagiello and J. Pérez-Ramírez, *Adv. Funct. Mater.*, 2016, **26**, 5621-5630.
- R. Warringham, S. Mitchell, R. Murty, R. Schäublin, P. Crivelli, J. Kenvin and J. Pérez-Ramírez, *Chem. Mater.*, 2017, **29**, 4052-4062.
- J. Rowlinson and B. Widom, *Molecular Theory of Capillarity (Clarendon, Oxford)*, 1982.
- P. Tarazona and R. Evans, *Mol. Phys.*, 1984, **52**, 847-857.
- P. Tarazona, U. M. B. Marconi and R. Evans, *Mol. Phys.*, 1987, **60**, 573-595.
- N. Seaton, J. Walton and N. Quirke, *Carbon*, 1989, **27**, 853-861.
- C. Lastoskie, K. E. Gubbins and N. Quirke, *Journal of Physical Chemistry*, 1993, **97**, 4786-4796.
- P. A. Monson, *Microporous Mesoporous Mater.*, 2012, **160**, 47-66.
- R. T. Cimino, P. Kowalczyk, P. I. Ravikovitch and A. V. Neimark, *Langmuir*, 2017, **33**, 1769-1779.
- C. T. Kresge, M. E. Leonowicz, W. J. Roth, J. C. Vartuli and J. S. Beck, *Nature*, 1992, **359**, 710-712.
- M. Thommes, in *Nanoporous Materials: Science and Engineering*, Imperial College Press 2004, vol. Volume 4, pp. 317-364.
- W. Schwieger, A. G. Machoke, T. Weissenberger, A. Inayat, T. Selvam, M. Klumpp and A. Inayat, *Chem. Soc. Rev.*, 2016, **45**, 3353-3376.
- J. Pérez-Ramírez, C. H. Christensen, K. Egeblad, C. H. Christensen and J. C. Groen, *Chem. Soc. Rev.*, 2008, **37**, 2530-2542.
- M. Hartmann and W. Schwieger, *Chem. Soc. Rev.*, 2016, **45**, 3311-3312.
- G. Mason and D. H. Everett, *Proceedings of the Royal Society of London. A. Mathematical and Physical Sciences*, 1983, **390**, 47-72.
- J. Ruiz-Martínez, A. M. Beale, U. Deka, M. G. O'Brien, P. D. Quinn, J. F. W. Mosselmans and B. M. Weckhuysen, *Angew. Chem. Int. Ed.*, 2013, **52**, 5983-5987.
- E. T. C. Vogt and B. M. Weckhuysen, *Chem. Soc. Rev.*, 2015, **44**, 7342-7370.
- S. Peng, Q.-H. Hu, S. Dultz and M. Zhang, *Journal of Hydrology*, 2012, **s 472-473**, 254-261.
- A. H. Janssen, A. J. Koster and K. P. de Jong, *Angew. Chem. Int. Ed.*, 2001, **40**, 1102-1104.
- K. P. de Jong, J. Zečević, H. Friedrich, P. E. de Jongh, M. Bulut, S. van Donk, R. Kenmogne, A. Finiels, V. Hulea and F. Fajula, *Angew. Chem. Int. Ed.*, 2010, **49**, 10074-10078.
- K. S. Rao, *J. Phys. Chem.*, 1941, **45**, 500-506.
- K. S. Rao, *J. Phys. Chem.*, 1941, **45**, 506-512.
- K. S. Rao, *J. Phys. Chem.*, 1941, **45**, 513-517.
- G. A. Tompsett, L. Krogh, D. W. Griffin and W. C. Conner, *Langmuir*, 2005, **21**, 8214-8225.
- R. Riedel, G. Mera, R. Hauser and A. Klönczynski, *J. Ceram. Soc. Jpn.*, 2006, **114**, 425-444.
- P. Colombo, *Polymer Derived Ceramics: From Nanostructure to Applications*, DEStech Publications, 2010.
- P. Colombo, G. Mera, R. Riedel and G. D. Sorarù, *J. Am. Ceram. Soc.*, 2010, **93**, 1805-1837.
- K. Lu, *Materials Science and Engineering: R: Reports*, 2015, **97**, 23-49.
- R. M. Prasad, Y. Jüttke, H. Richter, I. Voigt, R. Riedel and A. Gurlo, *Adv. Eng. Mater.*, 2016, **18**, 721-727.
- P. Lu, Q. Huang, B. Liu, Y. Bando, Y.-L. Hsieh and A. K. Mukherjee, *J. Am. Chem. Soc.*, 2009, **131**, 10346-10347.
- M. Wilamowska-Zawlocka, P. Puczkarski, Z. Grabowska, J. Kaspar, M. Graczyk-Zajac, R. Riedel and G. D. Sorarù, *RSC Advances*, 2016, **6**, 104597-104607.
- D. Assefa, E. Zera, R. Campostrini, G. D. Soraru and C. Vakifahmetoglu, *Ceram. Int.*, 2016, **42**, 11805-11809.
- G. D. Soraru, F. Dalcanale, R. Campostrini, A. Gaston, Y. Blum, S. Carturan and P. R. Aravind, *J. Mater. Chem.*, 2012, **22**, 7676-7680.
- P. Vallachira Warriam Sasikumar, E. Zera, M. Graczyk-Zajac, R. Riedel and G. D. Soraru, *J. Am. Ceram. Soc.*, 2016, **99**, 2977-2983.

55. V. S. Pradeep, Ph.D. Ph.D., University of Trento, 2013.
56. J. S. Downey, G. Mclsaac, R. S. Frank and H. D. H. Stöver, *Macromolecules*, 2001, **34**, 4534-4541.
57. A. Tamayo, M. A. Mazo, R.-C. Roberto, A. Martin-Illana, L. Bedoya, M. Veiga and J. Rubio, *Chem. Eng. J.*, 2015, **280**.
58. C. Vakifahmetoglu, D. Zeydanli, V. C. Ozalp, B. A. Borsa and G. D. Soraru, *Materials & Design*, 2018, **140**, 37-44.
59. J. M. Rosenholm, C. Sahlgren and M. Lindén, *Curr. Drug Targets*, 2011, **12**, 1166-1186.
60. T. Konegger, L. F. Williams and R. K. Bordia, *J. Am. Ceram. Soc.*, 2015, **98**, 3047-3053.
61. Y. Blum, G. D. Sorarù, A. P. Ramaswamy, D. Hui and S. M. Carturan, *J. Am. Ceram. Soc.*, 2013, **96**, 2785-2792.
62. V. S. Pradeep, D. G. Ayana, M. Graczyk-Zajac, G. D. Soraru and R. Riedel, *Electrochim. Acta*, 2015, **157**, 41-45.
63. S. Aguirre-Medel, P. Jana, P. Kroll and G. D. Sorarù, *Materials*, 2018, **11**, 2589.
64. C. A. Schneider, W. S. Rasband and K. W. Eliceiri, *Nat. Methods*, 2012, **9**, 671-675.
65. M. Luisa Ojeda, J. Marcos Esparza, A. Campero, S. Cordero, I. Kornhauser and F. Rojas, *PCCP*, 2003, **5**, 1859-1866.
66. J. Jagiello, C. Ania, J. B. Parra and C. Cook, *Carbon*, 2015, **91**, 330-337.
67. G. Horvath and K. Kawazoe, *J. Chem. Eng. Jpn.*, 1983, **16**, 470-475.
68. Q. Xiong, T. G. Baychev and A. P. Jivkov, *J. Contam. Hydrol.*, 2016, **192**, 101-117.
69. K. Morishige and M. Ishino, *Langmuir*, 2007, **23**, 11021-11026.
70. P. Bertier, K. Schweinar, H. Stanjek, A. Ghanizadeh, C. Clarkson, A. Busch, N. Kampman, D. Prinz, A. Amann, B. Krooss and V. Pipich, *CMS Workshop Lectures*, 2016, **21**, 151-161.
71. F. Rouquerol, J. Rouquerol, K. S. Sing, P. Llewellyn and G. Maurin, *Adsorption by powders and porous solids : principles, methodology and applications*, 2014.
72. D. H. Everett, G. D. Parfitt, K. S. Sing and R. Wilson, *J. App. Chem. Biotech.*, 1974, **24**, 199-219.
73. J. Choma and M. Jaroniec, *Adsorption Science & Technology*, 2001, **19**, 765-776.
74. J. C. Lang, J. Kenvin, J. T. Lee, J. Jiang and D. W. Armstrong, personal communication.
75. N. Seaton, *Chem. Eng. Sci.*, 1991, **46**, 1895-1909.
76. M. Thommes, B. Smarsly, M. Groenewolt, P. I. Ravikovitch and A. V. Neimark, *Langmuir*, 2006, **22**, 756-764.
77. J. T. Park, D. K. Roh, R. Patel, E. Kim, D. Y. Ryu and J. H. Kim, *J. Mater. Chem.*, 2010, **20**, 8521-8530.
78. J.-H. Sun, Z. Shan, T. Maschmeyer and M.-O. Coppens, *Langmuir*, 2003, **19**, 8395-8402.
79. K. Nakanishi, *J. Porous Mater.*, 1997, **4**, 67-112.